

# Where to Place a Heavy Payload on a Multirotor UAV for Best Control Performance

Sander Doodeman <sup>a</sup>, Paula Chanfreut Palacio <sup>a</sup>, Elena Torta <sup>a</sup>, Duarte Antunes <sup>a</sup>

<sup>a</sup>*Department of Mechanical Engineering, TU/e, Eindhoven University of Technology, Eindhoven, The Netherlands*

## Abstract

This paper studies the impact of rigidly attached heavy payload placement - where the payload mass significantly influences the UAV's dynamics - on the stability and control performance of a multirotor unmanned aerial vehicle (UAV). In particular, we focus on how the position of such a payload relative to the vehicle's Center of Gravity ( $CoG$ ) affects the stability and control performance at an arbitrary point of interest on the UAV, such as the payload position, and on how this position can be optimized. Our conclusions are based on two key contributions. First, we analyze the stability of the zero-dynamics of a complete nonlinear model of the UAV with payload. We demonstrate that the stability of the zero dynamics depends on the vertical signed distance in the body-fixed frame between the controlled output position and the combined  $CoG$  of the UAV with payload. Specifically, positioning the output below the  $CoG$  yields unstable zero dynamics, while the linearized zero dynamics are marginally stable when placing it above, indicating reduced sensitivity to input disturbances. Second, we analyze the performance of the linearized UAV model with payload by providing an analytical expression for the  $\mathcal{H}_2$ -norm, from which we can quantify the system's attenuation to white noise input disturbances. We conclude that less control authority leads to a higher optimal position of the controlled output with respect to the  $CoG$  for closed-loop white-noise disturbance rejection capabilities, also when the heavy payload is the controlled output. The results are illustrated through numerical examples.

**Key words:** Application of nonlinear analysis and design; Multirotor UAV; Disturbance rejection;  $\mathcal{H}_2$ -norm optimization.

## 1 Introduction

With recent advances in control and perception technologies, multirotor Unmanned Aerial Vehicles (UAVs) have become increasingly viable for a wide range of real-world applications. UAVs are now used for tasks such as window cleaning, where tethered drones are equipped with spraying systems [8, 12, 24], and in precision agriculture, where they are used to spray and monitor crops [5, 10]. The growing size and payload capacity of modern drones have also enabled their use in package delivery [1, 2]. Another emerging area is non-destructive testing (NDT), in which drones carry heavy inspection tools such as X-ray devices to perform autonomous structural evaluations [13, 15]. In some cases, UAVs are even equipped with robotic manipulators to interact with the environment and perform complex manipulation tasks [18, 19]. Whereas some tasks involve heavy tools that need to be carried by the UAV, others require a long flight time, leading to increased battery capacity and weight. Determining the optimal placement of these components on the UAV is important,

as it directly affects stability and control performance. This is particularly important for tasks that require the UAV to maintain a precise hover, such as in NDT or window cleaning, where accurate positioning is essential for achieving the tasks. In that regard, it is preferable to horizontally balance the total Center of Gravity ( $CoG$ ) of the system in the center of the UAV with respect to the rotors, since otherwise, the rotors need to rotate at different speeds, reducing the efficiency. This preference for  $CoG$  balance has been discussed in multiple studies [16, 20]. However, many of these studies only consider the stability of the  $CoG$  of the UAV, while for complex tasks, another point on the UAV, such as the payload position, must be accurately controlled. Another important point is that in many applications where payload position optimization is relevant, the UAV is controlled around a hovering state to achieve accurate positioning (e.g., window cleaning or X-ray inspection). In these applications, one can assume that drone state and inputs take values close to those in hover operation and even perform analyses based on linearized models.

In this paper, we aim to understand where to (optimally) place a rigidly attached heavy payload with respect to

*Email address:* s.doodeman@tue.nl (Sander Doodeman).

the *CoG* of a multirotor UAV (such as a quadcopter or hexacopter) from a control point of view, taking into account that the to be controlled position of interest in the UAV can be arbitrary and thus can also be the payload position. We present a twofold contribution to the stability and performance analysis of a multirotor UAV with a heavy payload.

- First, using a zero dynamics analysis, we demonstrate that when the controlled output position lies below the combined *CoG* of the UAV with the payload, the zero dynamics are unstable, while the linearized zero dynamics are marginally stable when placing it below this *CoG*, indicating increased sensitivity to input disturbances when the payload is below the *CoG* of the UAV. An important consequence is that, if one is interested in accurately controlling the position of a UAV payload, it is better to place the payload above the *CoG* of the UAV instead of below.
- Second, we conduct a quantitative performance analysis based on the linearized UAV model with payload to quantify how physical parameters — such as payload mass, payload position, and inertial properties — affect the closed-loop disturbance rejection capabilities of the system. To this effect, we derive an analytical expression for the  $\mathcal{H}_2$ -norm measuring the output attenuation to input white noise disturbances. These input disturbances can arise due to motor actuation delays of the rotors and unmodeled aerodynamic effects, for example. From this expression, we derive the optimal position of the controlled output with respect to the *CoG* as a function of a cost parameter specifying control authority. This expression reveals that the less the allowed controlled authority in the cost, the higher the controlled output position should be placed with respect to the *CoG*. The expression not only further reveals that, if the payload is the controlled output, the payload should be placed above the *CoG* rather than below the *CoG* for best input noise attenuation (coherent with the zero-dynamics analysis), but also quantifies the attenuation in both cases as a function of the system parameters.

Some related results appear in the literature. In [4], it is discussed that for forward flight stability, a *CoG* below the rotor plane will result in a more stable flight, since the flight wind will result in a stabilizing torque. However, this study also mentions that a higher *CoG* could result in better wind disturbance rejection. These remarks hold for a linearized system, but these statements are not backed up with formal analyses. In [17], an analysis based on the zero-dynamics of a quadrotor UAV is used to conclude that when the position of a payload with negligible mass is to be controlled and its position is the point of interest, it is better to have this point of interest above the UAV. When the payload is above the *CoG* of the UAV and it has to move in one horizontal direction, the UAV will tilt towards that direction, bringing the payload closer to its desired direction. The

opposite is true when the payload is below the UAV. With respect to [17], in our work, the point of interest can lie anywhere on the UAV, and we also investigate how the mass of the payload will influence the stability and performance of the system. Removing this assumption that the mass of the payload is negligible leads to a significantly different system, namely in terms of the effect of the torque applied to the multirotor UAV, which induces a translational acceleration on the *CoG* when this *CoG* is not at the center point of the rotors. Furthermore, we focus not only on the stability of the zero dynamics as in [17], but also on the difference in performance for different payload configurations and different system parameters. This quantitative analysis using the  $\mathcal{H}_2$  norm has, to the best of our knowledge, not been carried out in the literature.

It should be noted that the placement of a heavy payload is, in some cases, determined by practical aspects. For package delivery, it is useful to hold the package under the UAV, and a down-facing camera should also be under the UAV. Other tasks, such as aerial manipulation and NDT inspection, provide more flexibility in the payload placement. Therefore, this work can serve as a guide for choosing the position of heavy, or task-specific components on a multirotor UAV.

This paper is organized as follows: A dynamic model of a multirotor UAV with a heavy payload is derived in Section 2. The zero dynamics for the output position and yaw are analyzed in Section 3, which depend on this chosen output position and the position of the heavy payload. In Section 4 a system linearization is performed, from which, using optimal control methods, an analytical expression is derived for the  $\mathcal{H}_2$ -norm for when the output position is above or below the combined center of gravity (*CoG*) of the system, showing that the  $\mathcal{H}_2$ -norm is always smaller when the output is above the *CoG* of the UAV. In Section 5, simulations of the nonlinear system are compared with simulations of the linearized system to show the validity of the conclusions of the previous sections for both the nonlinear and linearized system.

## 2 Euler-Lagrange Dynamic Model

Let  $S(\cdot)$  be a skew-symmetric matrix such that  $S(a)b = a \times b$  for  $a \in \mathbb{R}^3$  and  $b \in \mathbb{R}^3$ . The Kronecker product between two matrices is denoted by  $\otimes$ . Let  $I_d$  be the  $d \times d$  identity matrix and  $\mathbf{e}_1$ ,  $\mathbf{e}_2$ , and  $\mathbf{e}_3$  be the unit vectors along each axis of a coordinate frame, such that  $\mathbf{e}_1 = \begin{bmatrix} 1 & 0 & 0 \end{bmatrix}^\top$ ,  $\mathbf{e}_2 = \begin{bmatrix} 0 & 1 & 0 \end{bmatrix}^\top$ ,  $\mathbf{e}_3 = \begin{bmatrix} 0 & 0 & 1 \end{bmatrix}^\top$ . We further define  $g \approx 9.81 \text{ [m/s}^2\text{]}$  as the gravitational acceleration.

For the dynamic model of the UAV, we consider a multirotor UAV, which can, for example, be a quadcopter

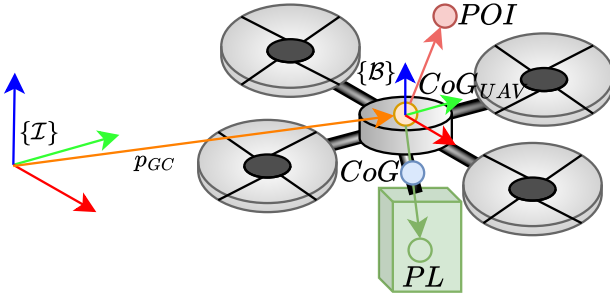


Fig. 1. Considered coordinate frames and relevant positions or a hexacopter, with a rigidly attached heavy payload. On this UAV, we define four relevant points (see Fig. 1):

- The Center of Gravity of the UAV ( $CoG_{UAV}$ ) without payload, which also coincides with the center point of the rotor plane, defined by the center of the circle on which all rotors are located.
- The payload position ( $PL$ ).
- The Center of Gravity ( $CoG$ ) for the UAV with payload mass (which is shifted with respect to the  $CoG_{UAV}$  due to the payload).
- The Point Of Interest ( $POI$ ), which is the to be controlled output position.

The choice of these relevant points on the UAV allows us to represent a UAV with multiple payloads as well, considering these as one composite payload, with a center of mass in  $PL$ .

**Remark 1** As mentioned in the Introduction, for the efficiency of the multirotor UAV, it is beneficial to have the  $CoG$  in the center of the UAV with respect to the rotors.

Let us define the mass of the UAV excluding payload as  $m_{UAV}$  and the mass of the payload as  $m_{PL}$ . The inertia of the UAV's body and payload with respect to the body-fixed frame is given by  $H_{UAV}$  and  $H_{PL}$ , respectively. The combined mass and inertia of the UAV's body and payload are given by  $m_{\text{tot}} = m_{UAV} + m_{PL}$  and  $H_{\text{tot}} = H_{UAV} + H_{PL}$ , respectively. For the derivation of the dynamic model, let  $\mathbf{p}_{UAV} \in \mathbb{R}^3$  be the position of the UAV's  $CoG_{UAV}$ , also defined as the centroid of the rotor positions, with respect to the inertial frame  $\mathcal{I}$ , indicated in Fig. 1. Furthermore, let  $R$  indicate the rotation matrix that describes the rotation of the body-fixed frame  $\mathcal{B}$ , with  $CoG_{UAV}$  as its origin, of the UAV with respect to the inertial frame  $\mathcal{I}$ . We are interested in the positions of the  $POI$  and payload with respect to  $\mathcal{B}$ . Let us define these positions as

$$\mathbf{r}_{POI} = \begin{bmatrix} x_{POI} \\ y_{POI} \\ z_{POI} \end{bmatrix}, \quad \mathbf{r}_{PL} = \begin{bmatrix} x_{PL} \\ y_{PL} \\ z_{PL} \end{bmatrix},$$

respectively with respect to the UAV in the body-fixed frame  $\mathcal{B}$ . We then define the position of the  $POI$   $\mathbf{p}_{POI} \in \mathbb{R}^3$  and the center of the rigidly attached payload  $\mathbf{p}_{PL} \in \mathbb{R}^3$  in the inertial frame  $\mathcal{I}$  as

$$\begin{aligned} \mathbf{p}_{POI} &= \mathbf{p}_{UAV} + R\mathbf{r}_{POI}, \\ \mathbf{p}_{PL} &= \mathbf{p}_{UAV} + R\mathbf{r}_{PL}. \end{aligned}$$

The position of the  $CoG$   $\mathbf{p}_{CoG} \in \mathbb{R}^3$  of the total system can then be proven to be

$$\begin{aligned} \mathbf{p}_{CoG} &= \frac{m_{UAV}}{m_{\text{tot}}} \mathbf{p}_{UAV} + \frac{m_{PL}}{m_{\text{tot}}} \mathbf{p}_{PL} \\ &= \mathbf{p}_{UAV} + \frac{m_{PL}}{m_{\text{tot}}} R\mathbf{r}_{PL}, \end{aligned}$$

which is the weighted average of the individual centers of gravity  $\mathbf{p}_{UAV}$  and  $\mathbf{p}_{PL}$ . If we then define  $\hat{\mathbf{r}}$  as

$$\hat{\mathbf{r}} = \mathbf{r}_{POI} - \frac{m_{PL}}{m_{\text{tot}}} \mathbf{r}_{PL}$$

we can express the position of the  $CoG$  as function of the position of the  $POI$

$$\mathbf{p}_{CoG} = \mathbf{p}_{POI} - R\hat{\mathbf{r}}$$

By utilizing the parallel axis theorem [6], the total inertia at the  $CoG$ ,  $H_{CoG}(\mathbf{r}_{PL})$ , is then given by

$$\begin{aligned} H_{CoG}(\mathbf{r}_{PL}) &= m_{UAV} S\left(-\frac{m_{PL}}{m_{\text{tot}}} \mathbf{r}_{PL}\right)^\top S\left(-\frac{m_{PL}}{m_{\text{tot}}} \mathbf{r}_{PL}\right) \\ &\quad + m_{PL} S\left(\frac{m_{UAV}}{m_{\text{tot}}} \mathbf{r}_{PL}\right)^\top S\left(\frac{m_{UAV}}{m_{\text{tot}}} \mathbf{r}_{PL}\right) + H_{\text{tot}} \\ &= \frac{m_{UAV} m_{PL}}{m_{\text{tot}}} S(\mathbf{r}_{PL})^\top S(\mathbf{r}_{PL}) + H_{\text{tot}}. \end{aligned} \tag{1}$$

We further define the Euler angles  $\boldsymbol{\eta} = [\varphi \ \theta \ \psi]^\top$  that result in the rotation matrix  $R$  using the Euler ZYX (yaw-pitch-roll) convention, rotating vectors from the body-fixed frame to a global frame, and  $\boldsymbol{\omega} = [\omega_x \ \omega_y \ \omega_z]^\top$  as the body-fixed rotational velocity. Furthermore, the relation between the time derivative of the rotation matrix  $\dot{R}$  and the rotational velocity  $\boldsymbol{\omega}$  is given by  $\dot{R} = RS(\boldsymbol{\omega})$  and the relation between  $\boldsymbol{\omega}$  and Euler angles  $\dot{\boldsymbol{\eta}}$  is given by

$$\boldsymbol{\omega} = \Gamma \dot{\boldsymbol{\eta}}, \quad \Gamma = \begin{bmatrix} 1 & 0 & -\sin(\theta) \\ 0 & \cos(\varphi) & \sin(\varphi) \cos(\theta) \\ 0 & -\sin(\varphi) & \cos(\varphi) \cos(\theta) \end{bmatrix}.$$

The control inputs for the UAV are given by

$$\mathbf{u} = M_F(\boldsymbol{\eta}) \mathbf{F}_u, \quad M_F(\boldsymbol{\eta}) := \begin{bmatrix} Re_3 & 0_{3 \times 3} \\ \mathbf{0} & I_3 \end{bmatrix},$$

where  $\mathbf{F}_u = [T \ \tau_\varphi \ \tau_\theta \ \tau_\psi]^\top$  is the control input vector. Here,  $T$  denotes the thrust magnitude for the thrust vector  $T\mathbf{e}_3^B$ , and  $\tau_\varphi$ ,  $\tau_\theta$ , and  $\tau_\psi$  indicate the rotational torques. Here,  $\mathbf{e}_3^B$  is the unit vector  $\mathbf{e}_3$  in the body-fixed frame  $\mathcal{B}$ . A control allocation matrix can transform these thrust and torques into the desired rotor speeds for different rotor configurations, e.g., for a quadcopter or hexacopter [21].

The dynamic model of the UAV with payload is derived using a Lagrangian approach [11, 14], assuming the payload is static. Here, we first define the kinetic energy  $\mathcal{K}$  and the potential energy  $\mathcal{U}$  for the *CoG* of the UAV:

$$\begin{aligned}\mathcal{K} &= \frac{1}{2}m_{\text{tot}}\dot{\mathbf{p}}_{CoG}^\top\dot{\mathbf{p}}_{CoG} + \frac{1}{2}\boldsymbol{\omega}^\top H_{CoG}(\mathbf{r}_{PL})\boldsymbol{\omega} \\ &= \frac{1}{2}m_{\text{tot}}\dot{\mathbf{p}}_{CoG}^\top\dot{\mathbf{p}}_{CoG} + \frac{1}{2}\dot{\boldsymbol{\eta}}^\top\Gamma^\top H_{CoG}(\mathbf{r}_{PL})\Gamma\dot{\boldsymbol{\eta}}, \\ \mathcal{U} &= m_{\text{tot}}g\mathbf{e}_3^\top\mathbf{p}_{CoG}.\end{aligned}\quad (2)$$

If we define  $\mathcal{L} = \mathcal{K} - \mathcal{U}$ , the Euler-Lagrange dynamic equations of the system are then given by

$$\frac{d}{dt}\frac{\partial\mathcal{L}}{\partial\dot{\xi}_i} - \frac{\partial\mathcal{L}}{\partial\xi_i} = u_i, \quad (3)$$

where  $\xi_i$  and  $u_i$  are the individual elements of the generalized coordinate vector  $\boldsymbol{\xi}$ , defined as  $\boldsymbol{\xi} = [\mathbf{p}_{POI}^\top \ \boldsymbol{\eta}^\top]^\top$ , and input vector  $\mathbf{u}$  respectively. This results in

$$\begin{aligned}&\begin{bmatrix} m_{\text{tot}}I_3 & m_{\text{tot}}RS(\hat{\mathbf{r}}) \\ m_{\text{tot}}\Gamma^\top S(\hat{\mathbf{r}})^\top R^\top & \Gamma^\top M_1 \end{bmatrix} \begin{bmatrix} \ddot{\mathbf{p}}_{POI} \\ \dot{\boldsymbol{\omega}} \end{bmatrix} + \\ &\begin{bmatrix} 0_{3\times 3} & m_{\text{tot}}RS(\boldsymbol{\omega})S(\hat{\mathbf{r}}) \\ m_{\text{tot}}\Gamma^\top M_2 R^\top & \Gamma^\top S(\boldsymbol{\omega})M_1 - \Gamma^\top M_3 \end{bmatrix} \begin{bmatrix} \dot{\mathbf{p}}_{POI} \\ \boldsymbol{\omega} \end{bmatrix} + \\ &\begin{bmatrix} m_{\text{tot}}g\mathbf{e}_3 \\ m_{\text{tot}}g\Gamma^\top S(\hat{\mathbf{r}})\Gamma\mathbf{e}_3 \end{bmatrix} = \begin{bmatrix} I_3 & 0_{3\times 3} \\ 0_{3\times 3} & \Gamma^\top \end{bmatrix} \mathbf{u},\end{aligned}$$

in which

$$\begin{aligned}M_1 &= H_{CoG}(\mathbf{r}_{PL}) + m_{\text{tot}}S(\hat{\mathbf{r}})^\top S(\hat{\mathbf{r}}), \\ M_2 &= S(\hat{\mathbf{r}})S(\boldsymbol{\omega}) - S(\boldsymbol{\omega})S(\hat{\mathbf{r}}), \\ M_3 &= m_{\text{tot}}(\Gamma^{-1}^\top \otimes \dot{\mathbf{p}}_{POI}^\top)R_\eta S(\hat{\mathbf{r}}) \\ R_\eta &= \begin{bmatrix} \frac{\partial R^\top}{\partial\varphi} & \frac{\partial R^\top}{\partial\theta} & \frac{\partial R^\top}{\partial\psi} \end{bmatrix}^\top.\end{aligned}$$

These equations of motion can be rewritten to

$$B_y(\boldsymbol{\eta}) \begin{bmatrix} \ddot{\mathbf{p}}_{POI} \\ \dot{\boldsymbol{\omega}} \end{bmatrix} + C_y(\dot{\mathbf{p}}_{POI}, \boldsymbol{\omega}, \boldsymbol{\eta}) \begin{bmatrix} \dot{\mathbf{p}}_{POI} \\ \boldsymbol{\omega} \end{bmatrix} + G_y(\boldsymbol{\eta}) = \mathbf{u}, \quad (4)$$

where

$$\begin{aligned}B_y(\boldsymbol{\eta}) &= \begin{bmatrix} m_{\text{tot}}I_3 & m_{\text{tot}}RS(\hat{\mathbf{r}}) \\ m_{\text{tot}}S(\hat{\mathbf{r}})^\top R^\top & M_1 \end{bmatrix}, \\ C_y(\dot{\mathbf{p}}_{POI}, \boldsymbol{\omega}, \boldsymbol{\eta}) &= \begin{bmatrix} 0_{3\times 3} & m_{\text{tot}}RS(\boldsymbol{\omega})S(\hat{\mathbf{r}}) \\ m_{\text{tot}}M_2 R^\top & S(\boldsymbol{\omega})M_1 - M_3 \end{bmatrix}, \\ G_y(\boldsymbol{\eta}) &= \begin{bmatrix} m_{\text{tot}}g\mathbf{e}_3 \\ m_{\text{tot}}gS(\hat{\mathbf{r}})\Gamma\mathbf{e}_3 \end{bmatrix},\end{aligned}$$

Finally, let us define the state  $\mathbf{x} = [\dot{\mathbf{p}}_{POI} \ \boldsymbol{\omega} \ \mathbf{p}_{POI} \ \boldsymbol{\eta}]^\top$ . The differential equation for the evolution of these states is then given by

$$\begin{aligned}\dot{\mathbf{x}} &= f(\mathbf{x}, \mathbf{F}_u) \\ &= \begin{bmatrix} B_y(\boldsymbol{\eta})^{-1}(\mathbf{u} - C_y(\dot{\mathbf{p}}_{POI}, \boldsymbol{\omega}, \boldsymbol{\eta}) \begin{bmatrix} \dot{\mathbf{p}}_{POI} \\ \boldsymbol{\omega} \end{bmatrix} - G_y(\boldsymbol{\eta})) \\ \begin{bmatrix} I_3 & 0_{3\times 3} \\ 0_{3\times 3} & \Gamma^{-1} \end{bmatrix} \begin{bmatrix} \dot{\mathbf{p}}_{POI} \\ \boldsymbol{\omega} \end{bmatrix} \end{bmatrix}.\end{aligned}\quad (5)$$

Note that if the mass of the payload were neglected, these equations of motion would coincide with the ones derived in [17]. Since this assumption is not made in the present paper, the model is a more general representation of the UAV system, allowing for investigating both the influence of the payload position as the point of interest on the UAV.

### 3 Zero dynamics analysis

The zero dynamics provide critical insight into the internal stability and performance limitations of a nonlinear system, such as the UAV with payload, [9]. These zero dynamics can be derived by performing an input-output linearization and then controlling the system's output to be zero. The remaining dynamics, the zero dynamics, can then be analyzed. These steps will be followed in this section.

We are interested in controlling the *POI*, as well as the yaw rate  $\omega_z$  in the body frame. Therefore, let us define the output of the system as

$$\begin{bmatrix} y_1 \\ y_2 \\ y_3 \\ y_4 \end{bmatrix} = \begin{bmatrix} \mathbf{p}_{POI} \\ \omega_z \end{bmatrix}.$$

Then, referring to (4), the inputs of the system appear in the first and second time derivatives of the output, specifically,

$$\begin{bmatrix} \ddot{y}_1 \\ \ddot{y}_2 \\ \ddot{y}_3 \\ \dot{y}_4 \end{bmatrix} = M_4(\boldsymbol{\eta})M_F(\boldsymbol{\eta})\mathbf{F}_u - M_4(\boldsymbol{\eta})M_5(\dot{\mathbf{p}}_{POI}, \boldsymbol{\omega}, \boldsymbol{\eta}), \quad (6)$$

with

$$\begin{aligned} M_4(\boldsymbol{\eta}) &= \begin{bmatrix} I_3 & 0_{3 \times 3} \\ 0_{1 \times 3} & \mathbf{e}_3^\top \end{bmatrix} B_y(\boldsymbol{\eta})^{-1}, \\ M_5(\dot{\mathbf{p}}_{POI}, \boldsymbol{\omega}, \boldsymbol{\eta}) &= C_y(\dot{\mathbf{p}}_{POI}, \boldsymbol{\omega}, \boldsymbol{\eta}) \begin{bmatrix} \dot{\mathbf{p}}_{POI} \\ \boldsymbol{\omega} \end{bmatrix} + G_y(\boldsymbol{\eta}). \end{aligned}$$

Here, it must be noted that  $B_y(\boldsymbol{\eta})$  is full rank, allowing for taking the inverse. This can be proven by showing that both  $m_{\text{tot}}I_3$  and its Schur complement  $B_y(\boldsymbol{\eta})/m_{\text{tot}}I_3$  are full rank [7]. This Schur complement is given by  $H_{CoG}(\mathbf{r}_{PL})$ , where this inertia matrix is full rank by definition. Since also  $m_{\text{tot}}I_3$  is full rank, then  $B_y(\boldsymbol{\eta})$  is full rank.

### 3.1 Input-output linearization

Let us now define the following input

$$\begin{aligned} \mathbf{F}_u^d(\dot{\mathbf{p}}_{POI}, \boldsymbol{\omega}, \boldsymbol{\eta}, \ddot{\mathbf{p}}_{POI,d}, \dot{\omega}_{z,d}) &= (M_4(\boldsymbol{\eta})M_F(\boldsymbol{\eta}))^{-1} \\ &\cdot \left( \begin{bmatrix} \ddot{\mathbf{p}}_{POI,d} \\ \dot{\omega}_{z,d} \end{bmatrix} + M_4(\boldsymbol{\eta})M_5(\dot{\mathbf{p}}_{POI}, \boldsymbol{\omega}, \boldsymbol{\eta}) \right), \end{aligned} \quad (7)$$

for the desired acceleration of the payload position  $\ddot{\mathbf{p}}_{POI,d}$  and the angular acceleration about the body-fixed  $z$ -axis  $\dot{\omega}_{z,d}$ . Substituting  $\mathbf{F}_u$  in (6) with  $\mathbf{F}_u^d$  from (7) will give us the input-output linearization such that

$$\begin{bmatrix} \ddot{\mathbf{p}}_{POI} \\ \dot{\omega}_z \end{bmatrix} = \begin{bmatrix} \ddot{\mathbf{p}}_{POI,d} \\ \dot{\omega}_{z,d} \end{bmatrix}.$$

### 3.2 Stability of zero dynamics

Let us first define the states  $z_1 = \omega_x$ ,  $z_2 = \omega_y$ ,  $z_3 = \phi$ ,  $z_4 = \theta$ ,  $z_5 = \psi$ . The transformation from these variables  $z_i$ , the outputs  $y_i$ , and the derivatives of the outputs in (6) to the state  $\mathbf{x}$  is a diffeomorphism. Let us also define the parameter  $\alpha$ , which plays a key role in this paper

and is defined as:

$$\begin{aligned} \alpha &= z_{POI} - z_{CoG} \\ &= z_{POI} - \frac{m_{PL}}{m_{\text{tot}}} z_{PL}. \end{aligned}$$

**Theorem 2** Consider the zero dynamics of states  $z_i$ , which have an equilibrium point at the origin ( $z_i = 0 \forall i$ ). Then the origin is unstable for  $\alpha < 0$ , and the linearized zero dynamics are marginally stable for  $\alpha \geq 0$ .

**PROOF.** We first set the output and its time derivatives to zero by implementing  $\ddot{\mathbf{p}}_{POI,d} = \mathbf{0}$  and  $\dot{\omega}_{z,d} = 0$  in (7), such that  $\ddot{\mathbf{p}}_{POI} = \dot{\mathbf{p}}_{POI} = \mathbf{p}_{POI} = \mathbf{0}$  and  $\dot{\omega}_z = \omega_z = 0$ . Implementing this in (4) gives us the zero dynamics for state vector  $\mathbf{z} = [z_1 \ z_2 \ z_3 \ z_4 \ z_5]^\top$ :

$$\begin{aligned} \dot{\mathbf{z}} &= f_{zd}(\mathbf{z}) \\ &= \begin{bmatrix} \begin{bmatrix} 0_{1 \times 3} & \mathbf{e}_1^\top \\ 0_{1 \times 3} & \mathbf{e}_2^\top \end{bmatrix} B_y(\mathbf{z}_\eta)^{-1} M_6 \\ \Gamma \boldsymbol{\omega}^0 \end{bmatrix}, \end{aligned} \quad (8)$$

with

$$\begin{aligned} M_6 &= M_F(\mathbf{z}_\eta) \mathbf{F}_u^d(\mathbf{0}, \boldsymbol{\omega}^0, \mathbf{z}_\eta, \mathbf{0}, 0) - M_5(\mathbf{0}, \boldsymbol{\omega}^0, \mathbf{z}_\eta), \\ \boldsymbol{\omega}^0 &= \begin{bmatrix} z_1 \\ z_2 \\ 0 \end{bmatrix}, \quad \mathbf{z}_\eta = \begin{bmatrix} z_3 \\ z_4 \\ z_5 \end{bmatrix}. \end{aligned}$$

The zero vector is a clear equilibrium point for this system and also the hovering point that we are interested in. The stability of this equilibrium point is analyzed by linearizing this system around it. The Jacobian  $J_{f_{zd}}$  is then given by

$$J_{f_{zd}} = \left. \frac{\partial f_{zd}(\mathbf{z})}{\partial \mathbf{z}} \right|_{\mathbf{z}=\mathbf{0}} = \begin{bmatrix} 0 & 0 & -\frac{g}{\alpha} & 0 & 0 \\ 0 & 0 & 0 & -\frac{g}{\alpha} & 0 \\ 1 & 0 & 0 & 0 & 0 \\ 0 & 1 & 0 & 0 & 0 \\ 0 & 0 & 0 & 0 & 0 \end{bmatrix}.$$

The eigenvalues of this Jacobian are  $-\sqrt{-\frac{g}{\alpha}}$ ,  $-\sqrt{-\frac{g}{\alpha}}$ ,  $0$ ,  $\sqrt{-\frac{g}{\alpha}}$ , and  $\sqrt{-\frac{g}{\alpha}}$ . From these expressions, it is clear that for  $\alpha < 0$ , all eigenvalues lie in the RHP, indicating unstable zero dynamics (see Fig. 2). In contrast, for a system where  $\alpha \geq 0$ , all eigenvalues lie on the imaginary axis, indicating Lyapunov stability for the linearized zero dynamics.

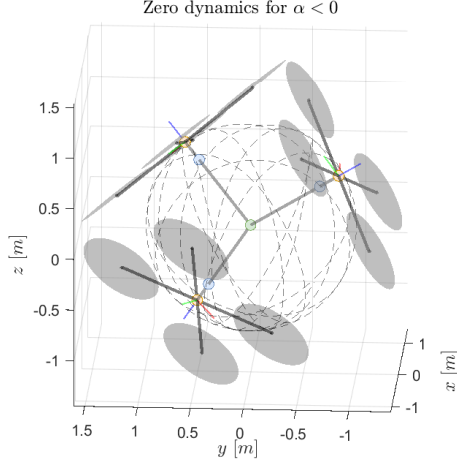


Fig. 2. Unstable zero dynamics simulations from (8) for when  $\alpha \approx -0.786 < 0$ , using the `ode45` solver in MATLAB. The green dot indicates the *POI*, which in this case coincides with the payload position, and the blue dot indicates the *CoG*.

**Remark 3** *Theorem 2 concludes marginal stability for the linearized zero dynamics, and not for the full zero dynamics in (8). Assuming a symmetric UAV (resulting in a diagonal inertia matrix), and a payload located exactly on the body-fixed  $z$ -axis, it can be shown that, the non-linearized zero dynamics reduce to*

$$\begin{bmatrix} \ddot{\phi} \\ \ddot{\theta} \\ \dot{\phi} \\ \dot{\theta} \end{bmatrix} = \begin{bmatrix} -\frac{\sin(\phi)(\hat{r}_z \cos(\phi)\dot{\theta}^2 + g \cos(\theta))}{\hat{r}_z} \\ -\frac{g \sin(\theta) - 2\phi\dot{\theta}\hat{r}_z \sin(\phi)}{\hat{r}_z \cos(\phi)} \\ \dot{\phi} \\ \dot{\theta} \end{bmatrix}.$$

*Due to the complexity and nonlinear terms in this expression, a stability analysis beyond that of the linearized system is not pursued in the present paper. Ongoing work focuses on the stability analysis of the zero dynamics for a planer reduction of the system. Nevertheless, simulations of the full zero dynamics hint towards Lyapunov stability, illustrated in Fig. 3, with the same initial conditions as in Fig. 2, and the parameters given in Table 1, except for  $z_{POI} = z_{PL} = -1.0$  for Fig. 2 and  $z_{POI} = z_{PL} = 1.0$  for Fig. 3.*

**Remark 4** *If we analyze the case where the payload position is the *POI* to be controlled, such that  $\alpha = \frac{m_{UAV}}{m_{tot}} z_{POI}$ , as shown in Fig. 4, it is better to have the payload above the UAV ( $z_{POI} \geq 0$ ). For the case where both the payload and *POI* positions have to be determined (as in Fig. 5), it is better if  $z_{POI} \geq \frac{m_{PL}}{m_{tot}} z_{PL}$ . These conclusions are in line with the conclusions for the case when the mass of the payload is negligible ( $m_{PL} = 0$ ), as drawn by [17].*

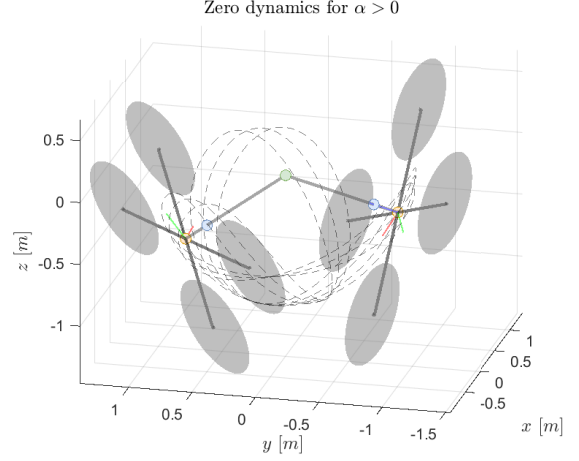


Fig. 3. Marginally stable (oscillating) zero dynamics simulations from (8) for when  $\alpha \approx 0.786 > 0$ , using the `ode45` solver in MATLAB. Again, the green dot indicates the *POI*, which in this case coincides with the payload position, and the blue dot indicates the *CoG*.

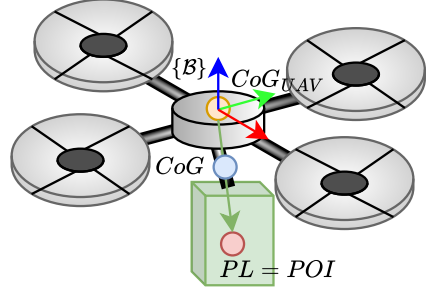


Fig. 4. Configuration where the payload position (*PL*) is the to be controlled position (*POI*)

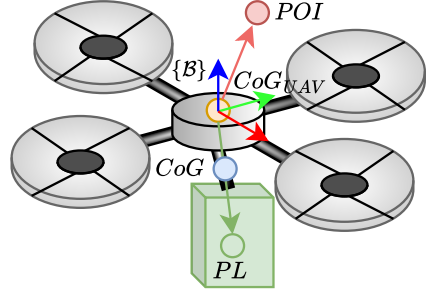


Fig. 5. Configuration where the payload position (*PL*) and the controlled position (*POI*) are free to choose

#### 4 Performance analysis of the linearized system

Since we are interested in hovering performance for the tasks that involve a heavy payload, the rotation of the UAV is limited. We therefore linearize the system to analyze the performance of the system and the disturbance rejection of the system for different positions of the *POI*

and payload. The performed linearization and assumptions are elaborated in Section 4.1. In Section 4.2, we then formulate the Optimal Control Problem (OCP) to obtain a quantitative analysis of the optimal positions of the *POI* and *PL*. From this, we derive an analytical formulation of the  $\mathcal{H}_2$ -norm in Section 4.3 to quantitatively analyze the white noise input disturbance rejection capabilities for the controlled output position.

#### 4.1 System linearization of a UAV with payload

Let us again consider the state  $\mathbf{x} = [\dot{\mathbf{p}}_{POI} \ \boldsymbol{\omega} \ \mathbf{p}_{POI} \ \boldsymbol{\eta}]^\top$ . The equilibrium point ( $\dot{\mathbf{x}} = 0$ ) for this system is given  $\mathbf{x}_{eq} = [\dot{\mathbf{p}}_{POI,eq} \ \boldsymbol{\omega}_{eq} \ \mathbf{p}_{POI,eq} \ \boldsymbol{\eta}_{eq}]^\top$ , where  $\dot{\mathbf{p}}_{POI,eq} = 0$ ,  $\boldsymbol{\omega}_{eq} = 0$ ,  $\mathbf{F}_{u,eq} = [m_{tot}g \ 0 \ 0 \ 0]^\top$ . This requires the third column of the rotation matrix  $R$  to be  $[0 \ 0 \ \pm 1]^\top$ , therefore,  $\varphi_{eq} = 0$ ,  $\theta_{eq} = 0$  ( $\varphi_{eq} = \pi$  and/or  $\theta_{eq} = \pi$  are also valid, but impractical). This leaves  $\mathbf{p}_{POI,eq}$  and the yaw  $\psi_{eq}$  free to choose. By means of a coordinate transformation by translation and a rotation over  $\psi$ , we can choose  $\mathbf{p}_{POI,eq} = 0$ ,  $\psi_{eq} = 0$  without loss of generality. Linearization around this equilibrium point gives

$$\dot{\mathbf{x}} = A_{lin}\mathbf{x} + B_{lin}\mathbf{F}_u^*, \quad (9)$$

with  $\mathbf{F}_u^* = \mathbf{F}_u - \mathbf{F}_{u,eq} = \begin{bmatrix} T^* & \tau_\varphi^* & \tau_\theta^* & \tau_\psi^* \end{bmatrix}^\top$  and

$$\begin{aligned} A_{lin} &= \frac{\partial f(\mathbf{x}, \mathbf{F}_u)}{\partial \mathbf{x}} \Big|_{\mathbf{x}=\mathbf{x}_{eq}, \mathbf{F}_u=\mathbf{F}_{u,eq}}, \\ B_{lin} &= \frac{\partial f(\mathbf{x}, \mathbf{F}_u)}{\partial \mathbf{F}_u} \Big|_{\mathbf{x}=\mathbf{x}_{eq}, \mathbf{F}_u=\mathbf{F}_{u,eq}}. \end{aligned}$$

To analyze the system above, we first introduce several assumptions for the linearized system.

**Assumption 5** *The sum of the inertias of the UAV's body and payload  $H_{tot}$  is diagonal, such that  $H_{tot} = \text{diag}(H_{tot,xx}, H_{tot,yy}, H_{tot,zz})$ .*

Due to the symmetry of most multirotor UAVs, this assumption is reasonable.

**Assumption 6** *The point of interest and the position of the payload are exactly above or below the CoG of the UAV body in the body-fixed frame, that is  $\mathbf{r}_{POI} = [0 \ 0 \ z_{POI}]^\top$  and  $\mathbf{r}_{PL} = [0 \ 0 \ z_{PL}]^\top$ , as visualized in Fig. 6.*

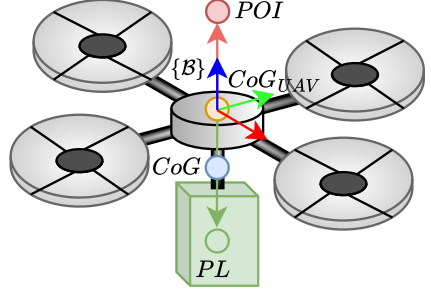


Fig. 6. Configuration of the *POI* and payload as in Assumption 6

Under these assumptions, (9) reduces to

$$\dot{\mathbf{x}} = \begin{bmatrix} g\theta \\ -g\varphi \\ 0_{4 \times 1} \\ \dot{\mathbf{p}}_{POI} \\ \boldsymbol{\omega} \end{bmatrix} + \begin{bmatrix} [0 \ 0 \ \alpha \ 0] \\ [0 \ -\alpha \ 0 \ 0] \\ I_4 \\ 0_{6 \times 4} \end{bmatrix} \hat{\mathbf{F}}_u, \quad (10)$$

with the same  $\alpha = z_{POI} - \frac{m_{PL}}{m_{tot}} z_{PL}$  as defined in Section 3, and  $\hat{\mathbf{F}}_u$  is a scaled input vector such that

$$\begin{aligned} \hat{\mathbf{F}}_u &= \begin{bmatrix} \hat{T} \\ \hat{\tau}_\varphi \\ \hat{\tau}_\theta \\ \hat{\tau}_\psi \end{bmatrix} = \Psi \mathbf{F}_u^*, \\ \Psi &= \begin{bmatrix} \frac{1}{m_{tot}} & 0 & 0 & 0 \\ 0 & \frac{m_{tot}}{b_2} & 0 & 0 \\ 0 & 0 & \frac{m_{tot}}{b_1} & 0 \\ 0 & 0 & 0 & \frac{1}{H_{tot,zz}} \end{bmatrix}, \end{aligned}$$

with

$$\begin{aligned} b_1 &= m_{PL}m_{UAV}z_{PL}^2 + H_{tot,yy}m_{tot}, \\ b_2 &= m_{PL}m_{UAV}z_{PL}^2 + H_{tot,xx}m_{tot}. \end{aligned} \quad (11)$$

This system can be decoupled for states

$$\mathbf{x}_1 = \begin{bmatrix} x_{POI} \\ \dot{x}_{POI} \\ \theta \\ \omega_y \end{bmatrix}, \quad \mathbf{x}_2 = \begin{bmatrix} y_{POI} \\ \dot{y}_{POI} \\ \varphi \\ \omega_x \end{bmatrix}, \quad \mathbf{x}_3 = \begin{bmatrix} z_{POI} \\ \dot{z}_{POI} \end{bmatrix}, \quad \mathbf{x}_4 = \begin{bmatrix} \psi \\ \omega_z \end{bmatrix},$$

simplifying the analysis for the position of the payload. The position of the payload only has an influence on the

dynamics for states  $\mathbf{x}_1$  and  $\mathbf{x}_2$ , which are given by

$$\begin{aligned}\dot{\mathbf{x}}_1 &= A_1 \mathbf{x}_1 + B_1 \hat{\tau}_\theta, \\ \dot{\mathbf{x}}_2 &= A_2 \mathbf{x}_2 + B_2 \hat{\tau}_\varphi,\end{aligned}\quad (12) \quad (13)$$

with

$$\begin{aligned}A_1 &= \begin{bmatrix} 0 & 1 & 0 & 0 \\ 0 & 0 & g & 0 \\ 0 & 0 & 0 & 1 \\ 0 & 0 & 0 & 0 \end{bmatrix}, \quad B_1 = \begin{bmatrix} 0 \\ \alpha \\ 0 \\ 1 \end{bmatrix}, \\ A_2 &= \begin{bmatrix} 0 & 1 & 0 & 0 \\ 0 & 0 & -g & 0 \\ 0 & 0 & 0 & 1 \\ 0 & 0 & 0 & 0 \end{bmatrix}, \quad B_2 = \begin{bmatrix} 0 \\ -\alpha \\ 0 \\ 1 \end{bmatrix}.\end{aligned}$$

**Remark 7** For both systems, the open-loop transfer function is given by

$$G(s) = \frac{\alpha s^2 + g}{s^2}.$$

When  $\alpha > 0$ , the zeros of this transfer function are  $s = \pm i\sqrt{\frac{g}{|\alpha|}}$ . For  $\alpha < 0$ , the zeros are  $s = \pm\sqrt{\frac{g}{|\alpha|}}$ .

The RHP zeros for  $\alpha < 0$  (i.e., the payload position is above the controlled output position) make this system a non-minimum phase system, leading to phase lag and decreased performance compared to when  $\alpha > 0$  (i.e., the payload position is below the controlled output position), which does not have RHP zeros. Remarkably, the RHP zeros for the linearized system coincide with the RHP poles of the linearized zero dynamics of the original non-linear system.

For the sake of completeness, the dynamic equations for  $\mathbf{x}_3$  and  $\mathbf{x}_4$  are given by

$$\dot{\mathbf{x}}_3 = A_3 \mathbf{x}_3 + B_3 \hat{T}, \quad (14)$$

$$\dot{\mathbf{x}}_4 = A_4 \mathbf{x}_4 + B_4 \hat{\tau}_\psi, \quad (15)$$

$$A_3 = A_4 = \begin{bmatrix} 0 & 1 \\ 0 & 0 \end{bmatrix}, \quad B_3 = B_4 = \begin{bmatrix} 0 \\ 1 \end{bmatrix}.$$

## 4.2 OCP formulation

With this linearized system representation, we now consider the following OCP with a quadratic cost function for the output of interest  $\mathbf{y}(t) = [\mathbf{p}_{POI}(t)^\top \ \psi(t)^\top]^\top$  and

for the input  $\hat{\mathbf{F}}_u(t)$ :

$$\begin{aligned}J &= \int_0^\infty \|\mathbf{y}(t)\|_Q^2 + \|\mathbf{F}_u^*(t)\|_R^2 dt \\ &= \int_0^\infty \|\mathbf{y}(t)\|_Q^2 + \|\Psi \hat{\mathbf{F}}_u(t)\|_R^2 dt,\end{aligned}\quad (16)$$

where  $Q = \text{diag}(q_1^2, q_2^2, q_3^2, q_4^2)$  and  $R = I$ , with  $q_i > 0$  for  $i \in \{1, 2, 3, 4\}$ . When considering the scaled input vector  $\hat{\mathbf{F}}_u$ , optimizing for  $J$  is equivalent to optimizing  $\hat{J}$ :

$$\hat{J} = \int_0^\infty \|\mathbf{y}(t)\|_{\hat{Q}}^2 + \|\hat{\mathbf{F}}_u(t)\|_R^2 dt, \quad (17)$$

with

$$\begin{aligned}\hat{Q} &= \text{diag}(\hat{q}_1^2, \hat{q}_2^2, \hat{q}_3^2, \hat{q}_4^2), \\ \hat{q}_1 &= \frac{b_1}{m_{\text{tot}}} q_1, \quad \hat{q}_2 = \frac{b_2}{m_{\text{tot}}} q_2, \\ \hat{q}_3 &= m_{\text{tot}} q_3, \quad \hat{q}_4 = H_{\text{tot},zz} q_4,\end{aligned}$$

Let us rearrange the state vector  $\mathbf{x}$  as  $\bar{\mathbf{x}} = [\mathbf{x}_1^\top \ \mathbf{x}_2^\top \ \mathbf{x}_3^\top \ \mathbf{x}_4^\top]^\top$  and such that we can define the output as

$$\mathbf{y} = \bar{C} \bar{\mathbf{x}},$$

where

$$\bar{C} = \begin{bmatrix} 1 & 0 & 0 & 0 & 0 & 0 & 0 & 0 & 0 & 0 & 0 & 0 \\ 0 & 0 & 0 & 0 & 1 & 0 & 0 & 0 & 0 & 0 & 0 & 0 \\ 0 & 0 & 0 & 0 & 0 & 0 & 0 & 0 & 1 & 0 & 0 & 0 \\ 0 & 0 & 0 & 0 & 0 & 0 & 0 & 0 & 0 & 0 & 0 & 1 \end{bmatrix}.$$

The optimal cost  $\hat{J}^*$  for the OCP can be formulated as  $\hat{J}^* = \|\bar{\mathbf{x}}\|_P^2$ , where  $P$  is the unique PSD solution to the Algebraic Riccati Equation (ARE) [23]. This cost matrix  $P$  gives the optimal cost for any initial condition and is also essential to determine the  $\mathcal{H}_2$ -norm, which is a standard performance analysis for input to output attenuation [3].

**Proposition 8** The unique PSD solution of  $P$  for the ARE, given the OCP in (17), for the linearized UAV with payload system in (9) is given in (18):

$$P = \begin{bmatrix} P_1 & 0 & 0 & 0 \\ 0 & P_2 & 0 & 0 \\ 0 & 0 & P_3 & 0 \\ 0 & 0 & 0 & P_4 \end{bmatrix}, \quad (18)$$

with

$$P_1 = \begin{bmatrix} p_{11,1} & p_{12,1} & p_{13,1} & p_{14,1} \\ p_{12,1} & p_{22,1} & p_{23,1} & p_{23,1} \\ p_{13,1} & p_{23,1} & p_{33,1} & p_{34,1} \\ p_{14,1} & p_{24,1} & p_{34,1} & p_{44,1} \end{bmatrix}, \quad (19)$$

$$P_2 = \begin{bmatrix} p_{11,2} & p_{12,2} & p_{13,2} & p_{14,2} \\ p_{12,2} & p_{22,2} & p_{23,2} & p_{23,2} \\ p_{13,2} & p_{23,2} & p_{33,2} & p_{34,2} \\ p_{14,2} & p_{24,2} & p_{34,2} & p_{44,2} \end{bmatrix}, \quad (20)$$

$$P_3 = \begin{bmatrix} \hat{q}_3 \sqrt{2\hat{q}_3} & \hat{q}_3 \\ \hat{q}_3 & \sqrt{2\hat{q}_3} \end{bmatrix}, \quad (21)$$

$$P_4 = \begin{bmatrix} \hat{q}_4 \sqrt{2\hat{q}_4} & \hat{q}_4 \\ \hat{q}_4 & \sqrt{2\hat{q}_4} \end{bmatrix}, \quad (22)$$

where matrix entries  $p_{mn,i}$  are given by

$$\begin{aligned} p_{11,i} &= \sqrt{\frac{2}{g}} \sqrt{\sqrt{2g\hat{q}_i^7} - \alpha\hat{q}_i^4 + \sqrt{2g\hat{q}_i^7 + \left(\sqrt{2g\hat{q}_i^7} - \alpha\hat{q}_i^4\right)^2}}, \\ p_{12,i} &= \frac{1}{2\hat{q}_i^2} p_{11,i}^2, \\ p_{13,i} &= \frac{g}{2\hat{q}_i^4} p_{11,i}^3 - gp_{22,i}, \\ p_{22,i} &= \frac{3}{8\hat{q}_i^4} p_{11,i}^3 + \frac{\alpha}{2g} p_{11,i} - \frac{\hat{q}_i^3}{gp_{11,i}}, \\ p_{23,i} &= \frac{g}{8\hat{q}_i^6} p_{11,i}^4, \\ p_{24,i} &= \frac{1}{\hat{q}_i} p_{11,i} - \alpha p_{22,i}, \\ p_{33,i} &= \frac{g}{2\hat{q}_i^4} p_{11,i}^2 \left( \frac{g}{2\hat{q}_i^4} p_{11,i}^3 - gp_{22,i} \right) - \frac{g}{\hat{q}_i} p_{11,i} + \alpha gp_{22,i}, \\ p_{34,i} &= \frac{g}{2\hat{q}_i^3} p_{11,i}^2 - \frac{\alpha g}{8\hat{q}_i^6} p_{11,i}^4, \\ p_{44,i} &= \frac{g}{2\hat{q}_i^5} p_{11,i}^3 - \frac{g}{\hat{q}_i} p_{22,i} - \alpha \left( \frac{1}{\hat{q}_i} p_{11,i} - \alpha p_{22,i} \right). \end{aligned}$$

**PROOF.** This proposition can be confirmed by simply substituting the solution for  $P$  in the ARE, given by

$$\begin{aligned} \bar{A}^\top P + P \bar{A} - P \bar{B} R^{-1} \bar{B}^\top P + \bar{Q} &= 0, \\ \bar{A} &= \text{diag}(A_1, A_2, A_3, A_4), \\ \bar{B} &= \text{diag}(B_1, B_2, B_3, B_4), \\ \bar{Q} &= \bar{C}^\top \bar{Q} \bar{C}, \end{aligned}$$

and checking this expression for  $P$ , where it can be proven that this particular solution for  $P$  is the only PSD

solution for the ARE, since the pair  $(\bar{A}, \bar{B})$  can easily be shown to be stabilizable and the pair  $(\bar{Q}, \bar{A})$  detectable and since  $R > 0$  [3].

The LQR optimal control law for the linearized system is then given by

$$\hat{F}_{u,LQR} = -R^{-1} \begin{bmatrix} 0 & 0 & B_3 & 0 \\ 0 & B_2 & 0 & 0 \\ B_1 & 0 & 0 & 0 \\ 0 & 0 & 0 & B_4 \end{bmatrix}^\top P \bar{x}. \quad (23)$$

#### 4.3 $\mathcal{H}_2$ -norm derivation and analysis

Considering the system's performance output chosen as  $\mathbf{z}(t) = [(\sqrt{Q}\mathbf{y}(t))^\top (\sqrt{R}\hat{F}_u(t))^\top]^\top$ , such that  $\|\mathbf{z}(t)\|^2 = \|\mathbf{y}(t)\|_Q^2 + \|\hat{F}_u(t)\|_R^2$ , we can define an expression for the  $\mathcal{H}_2$ -norm for each individual subsystem, since the linearized system is decoupled.

**Proposition 9** For subsystems  $i \in \{1, 2\}$  in (12) and (13), the  $\mathcal{H}_2$ -norm is given by

$$p_{14,i} = \hat{q}_i - \frac{\alpha \mathcal{H}_{11i}^2}{2\hat{q}_i^2}, \quad \frac{2a_i - b_i + \sigma_i}{q_i \sqrt{q_i} \sqrt{a_i - b_i + \sigma_i}}, \quad (24)$$

where

$$a_i = \sqrt{2g\hat{q}_i^7}, \quad b_i = \alpha\hat{q}_i^4, \quad \sigma_i = \sqrt{(a_i - b_i)^2 + a_i^2}.$$

For subsystems  $i \in \{3, 4\}$  in (14) and (15), the  $\mathcal{H}_2$ -norm is given by

$$\mathcal{H}_{2i} = \sqrt{2\hat{q}_i}. \quad (25)$$

**PROOF.** The  $\mathcal{H}_2$ -norm is given by  $\sqrt{\text{trace}(B_i^\top P_i B_i)}$  [25]. Using the expressions for the individual optimal control cost matrix in (19)-(22) for systems (12)-(15), we arrive at the above expressions.

From these expressions, we can optimize the  $\mathcal{H}_2$ -norm for the vertical positions of the *POI* and payload to obtain the following main result.

**Theorem 10** For the linearized system in (10), the optimal values for the vertical output position  $z_{POI}$  and the vertical payload position  $z_{PL}$  to minimize the  $\mathcal{H}_2$ -norm are given by  $z_{POI}^* = \sqrt{\frac{2g}{\hat{q}_i}}$  and  $z_{PL}^* = 0$ , respectively.

**PROOF.** Only the linearized subsystems (12) and (13) depend on the relevant vertical positions. In the expressions for the  $\mathcal{H}_2$ -norm, the output position  $z_{POI}$  only appears in  $\alpha$ . To derive the optimal output position in terms of the system parameters and the payload position  $z_{PL}$ , we first find the optimal value for  $\alpha$  by differentiating the  $\mathcal{H}_2$ -norm with respect to  $b_i$  (which directly depends on  $\alpha$ ). This gives

$$\begin{aligned} \frac{d\mathcal{H}_{2i}}{db_i} &= \frac{\frac{d\sigma_i}{db_i} - 1}{\hat{q}_i\sqrt{\hat{q}_i}\sqrt{a_i - b_i + \sigma_i}} - \frac{\left(\frac{d\sigma_i}{db_i} - 1\right)(2a_i - b_i + \sigma_i)}{2\hat{q}_i\sqrt{\hat{q}_i}(a_i - b_i + \sigma_i)^{\frac{3}{2}}}, \\ &= \frac{1}{\hat{q}_i\sqrt{\hat{q}_i}} \left( \frac{d\sigma_i}{db_i} - 1 \right) \left( \frac{\sigma_i - b_i}{2(a_i - b_i + \sigma_i)^{\frac{3}{2}}} \right), \\ &= \frac{1}{\hat{q}_i\sqrt{\hat{q}_i}} \left( \frac{b_i - a_i - \sigma_i}{\sigma_i} \right) \left( \frac{\sigma_i - b_i}{2(a_i - b_i + \sigma_i)^{\frac{3}{2}}} \right), \end{aligned}$$

since

$$\frac{d\sigma_i}{db_i} = \frac{b_i - a_i}{\sigma_i}.$$

Then,  $\frac{d\mathcal{H}_{2i}}{db_i} = 0$  gives  $b_i - a_i = \sigma_i$  and  $b_i = \sigma_i$ . Here,  $b_i - a_i = \sigma_i$  has no solutions for  $b_i$ , and  $b_i = \sigma_i$  has a solution for  $b_i = a_i$ . Since it can be proven that  $\frac{d\mathcal{H}_{2i}}{db_i} > 0$  for  $b_i > a_i$  and  $\frac{d\mathcal{H}_{2i}}{db_i} < 0$  for  $b_i < a_i$ ,  $b_i = a_i$  is the global minimum. To minimize the  $\mathcal{H}_2$ -norm, this results in an optimal value for

$$\alpha^* = \sqrt{\frac{2g}{\hat{q}_i}}.$$

Plugging this in for  $\mathcal{H}_{2i}$  in (24) gives  $a_i = b_i = \sigma_i$ , resulting in

$$\begin{aligned} \mathcal{H}_{2i} &= 2\sqrt{2g}\hat{q}_i^2 \\ &= 2q_i\sqrt{2g}\frac{b_i}{m_{tot}}. \end{aligned} \quad (26)$$

Looking at the expressions for  $b_i$  in (11), where  $z_{PL}$  appears quadratically, it is easy to prove that the optimal value for  $z_{PL}$  is given by  $z_{PL}^* = 0$ , resulting in  $z_{POI}^* = \alpha^* = \sqrt{\frac{2g}{\hat{q}_i}}$ .

**Remark 11** *From this analysis, we can conclude that having less control authority (a lower  $q_i$ ) results in a higher optimal value for  $\alpha$ . In other words, when the control authority is low, the further away the point of interest is from the CoG, the less influence input disturbances have on the position of the point of interest.*

**Remark 12** *If, e.g. for practical reasons, a heavy payload cannot be placed at its optimal position, which is at the CoG UAV, the optimal position of the to-be-placed point of interest is then given by  $z_{POI}^* = \sqrt{\frac{2g}{\hat{q}_i}} + \frac{m_{PL}}{m_{tot}}z_{PL}$ , considering the optimal value for  $\alpha$ .*

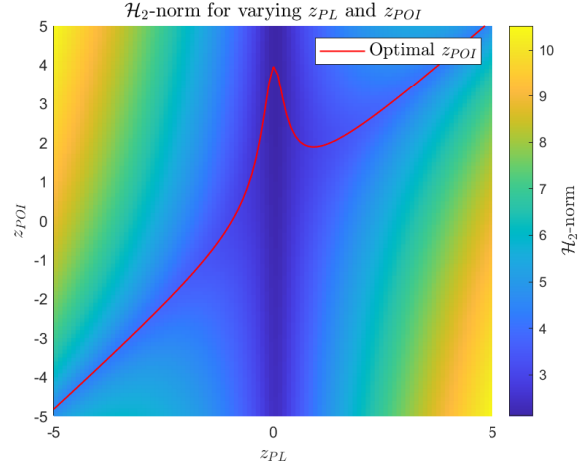


Fig. 7.  $\mathcal{H}_2$ -norm for varying  $z_{PL}$  and  $z_{POI}$ , verifying the optimal values  $z_{PL}^* = 0$  and  $z_{POI}^* = \sqrt{\frac{2g}{\hat{q}_i}} + z_{PL}$

For typical system parameters of a UAV (given in Table 1), and for  $q_1 = 5$ , the  $\mathcal{H}_2$ -norm is visualized in Fig. 7 for varying  $z_{PL}$  and  $z_{POI}$  for subsystem 1.

**Theorem 13** *The  $\mathcal{H}_2$ -norm for the linearized system in (12) and (13) for the OCP in (17) is smaller when the controlled output position (POI) is above the total CoG of the UAV (i.e.  $\alpha \geq 0$ ) compared to when the POI is below the CoG (i.e.  $\alpha < 0$ ).*

**PROOF.** Since Proposition 9 has shown that for (12) and (13), the  $\mathcal{H}_2$ -norm is equivalent, we will omit the subscript  $i$  from now on. Consider the difference between the  $\mathcal{H}_2$ -norm for these two cases, where for the above case  $b = \bar{b} = |b| \geq 0$ , and for the below case  $b = -\bar{b}$ :

$$\mathcal{H}_{2,\text{below}} - \mathcal{H}_{2,\text{above}} = \frac{2a + \bar{b} + \sigma_1}{\hat{q}\sqrt{\hat{q}}\sqrt{a + \bar{b} + \sigma_1}} - \frac{2a - \bar{b} + \sigma_2}{\hat{q}\sqrt{\hat{q}}\sqrt{a - \bar{b} + \sigma_2}},$$

where

$$\sigma_1 = \sqrt{(a + \bar{b})^2 + a^2}, \quad \sigma_2 = \sqrt{(a - \bar{b})^2 + a^2}.$$

To show that  $\mathcal{H}_{2,\text{below}} - \mathcal{H}_{2,\text{above}} > 0$ , we rewrite the inequality as

$$\frac{a + B_1}{\sqrt{B_1}} > \frac{a + B_2}{\sqrt{B_2}}, \quad (27)$$

where

$$B_1 = a + \bar{b} + \sigma_1, \quad B_2 = a - \bar{b} + \sigma_2. \quad (28)$$

Since  $\sigma_2 = \sqrt{(a - \bar{b})^2 + a^2} > \sqrt{(a - \bar{b})^2} = |a - \bar{b}|$ , we can state that  $B_2 > 0$ , and it is clear that  $B_2 > 0$  as well.

Therefore, multiplying by  $\sqrt{B_1}\sqrt{B_2}$  and rearranging the inequality gives:

$$\frac{a\sqrt{B_2} + B_1\sqrt{B_2}}{\sqrt{B_1}\sqrt{B_2}} > \frac{a\sqrt{B_1} + B_2\sqrt{B_1}}{\sqrt{B_1}\sqrt{B_2}}, \quad (29)$$

$$\left(\sqrt{B_1} - \sqrt{B_2}\right) \left(1 - \frac{a}{\sqrt{B_1}\sqrt{B_2}}\right) > 0.$$

Since  $B_1 > B_2 > 0$ , it remains to prove that  $a < \sqrt{B_1}\sqrt{B_2}$ . Taking the square on both sides gives

$$B_1B_2 > a^2,$$

which simplifies to

$$-\bar{b}^2 + a(\sigma_1 + \sigma_2) + \bar{b}(\sigma_2 - \sigma_1) + \sigma_1\sigma_2 > 0.$$

Multiplying by  $(\sigma_1 + \sigma_2) > 0$  gives

$$\begin{aligned} & -\bar{b}^2(\sigma_1 + \sigma_2) + a(\sigma_1 + \sigma_2)^2 \\ & + \bar{b}(\sigma_1^2 + \sigma_2^2) + \sigma_1\sigma_2(\sigma_1 + \sigma_2) > \\ & -\bar{b}^2(\sigma_1 + \sigma_2) + \sigma_1\sigma_2(\sigma_1 + \sigma_2) = \\ & (2a + \sigma_1 + \sigma_2)(\sigma_1\sigma_2 - \bar{b}^2) > 0. \end{aligned} \quad (30)$$

Since  $a > 0$ ,  $\sigma_1 > 0$ ,  $\sigma_2 > 0$  and  $\sigma_1\sigma_2 - \bar{b}^2 = \sqrt{4a^4 + \bar{b}^4} - \bar{b}^2 > \sqrt{\bar{b}^4} - \bar{b}^2 = 0$ , the above inequality holds, concluding the proof.

## 5 Simulation results

To verify the analytical results and investigate their validity for both the nonlinear and linearized systems, MATLAB simulations have been performed using the dynamic equations for the complete nonlinear system in (5) and the linearized system in (10), applying the control law in (23) for both systems. The system variables used for these simulations are shown in Table 1, which are chosen as realistic variables for a relatively large UAV. In Fig. 8, a typical trajectory is shown for different initial positions, where the position of the payload coincides with the point of interest of the system and is either above or below the *CoG*. To investigate the differences between the nonlinear and the linearized systems further, both systems are simulated for varying initial conditions. Since the nonlinearity of the system originates from the attitude angles, these initial conditions only vary for the initial attitude of the UAV. As expected, for larger angles, the difference between the nonlinear and linearized system is larger. Note that the error between the two system representations decreases due to the convergence to the origin. Fig. 10 shows the numerical validation of the analytical expression for the  $\mathcal{H}_2$ -norm for different values of  $\alpha$ , where  $\mathcal{H}_2$  indicates the noise amplification from the input to the corresponding

Table 1  
Used system variables

System parameter	Value
$g$	9.81 [m/s <sup>2</sup> ]
$m_{UAV}$	22.0 [kg]
$m_{PL}$	6.0 [kg]
$x_{PL}$	0.0 [m]
$y_{PL}$	0.0 [m]
$z_{PL}$	4.0 [m]
$x_{POI}$	0.0 [m]
$y_{POI}$	0.0 [m]
$z_{POI}$	4.0 [m]
$H_{\text{tot},xx}$	0.25 [kg · m <sup>2</sup> ]
$H_{\text{tot},yy}$	0.25 [kg · m <sup>2</sup> ]
$H_{\text{tot},zz}$	0.14 [kg · m <sup>2</sup> ]

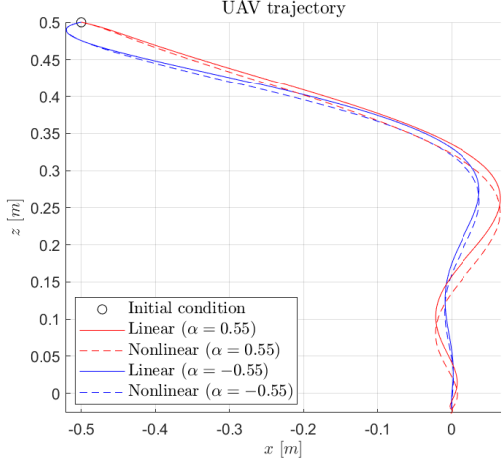


Fig. 8. UAV trajectory for the linearized and complete nonlinear system in (10) and (5) respectively, for the above- and below-configuration, using the `ode45` solver in MATLAB, with  $\mathbf{p}_0 = [-0.5 \ 0 \ 0.5]$  and  $q_i = 10$

outputs. The input for this system with white Gaussian noise input disturbances  $w(t) \sim \mathcal{N}(0, \sigma_w^2)$  is defined as

$$\mathbf{F}_u^* = -\Psi^{-1} \hat{\mathbf{F}}_{u,LQR} + w(t). \quad (31)$$

For the simulations of the complete nonlinear system with white noise disturbances on the inputs, the RK4 method was used [22]. In Fig. 10,  $\alpha$  indicates different distances between the payload (which is also in this case *POI*, as in Fig. 4) and the *CoG<sub>UAV</sub>*. In this figure, it can be seen that for the linearized system, the numerical values for the  $\mathcal{H}_2$ -norm coincide well with the analytical expression for different noise values. For the complete nonlinear system, the numerical values also match the analytical expression at lower noise levels, since the UAV's attitude deviation is lower. Furthermore, from the figure,

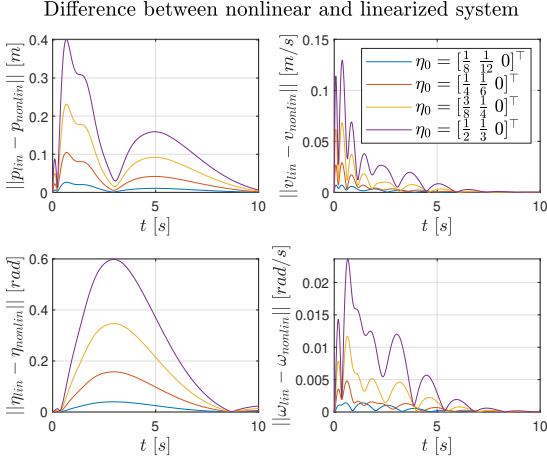


Fig. 9. Norm of the state error between the nonlinear and linearized system, showing that larger angles result in a larger difference between the two systems, using the `ode45` solver in MATLAB, for  $q_i = 10$

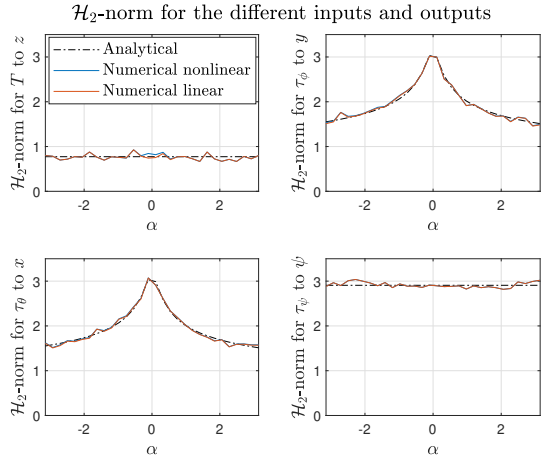


Fig. 10. Analytical and numerical values for the  $\mathcal{H}_2$ -norm for varying  $\alpha$ , showing that for both the simulated complete nonlinear and linearized system, the calculated  $\mathcal{H}_2$ -norm matches the analytical results, using an RK4 fixed-step simulation [22], for  $q_i = 5$  and input disturbances with  $\sigma_w = 0.1$ .

it is clear that the  $\mathcal{H}_2$ -norm is lower for positive values of  $\alpha$ , compared to its negative counterparts, in accordance with Theorem 13, also for the complete nonlinear system. Next, simulations of the nonlinear system in (5) have been performed with varying initial conditions and cost weights  $q_i$ , to verify that the cumulative costs as defined in (16) for the nonlinear system are always higher when  $\alpha < 0$  compared to when  $\alpha > 0$ . In these simulations, for each initial condition and cost weight  $q_i$ , the system was simulated using MATLAB's `ode45` function for  $\alpha = |\alpha|$  and  $\alpha = -|\alpha|$ . From Fig. 11, it is clear that for all simulated cases, it is still preferable to have  $\alpha > 0$ , similar to as was proven for the linearized system.

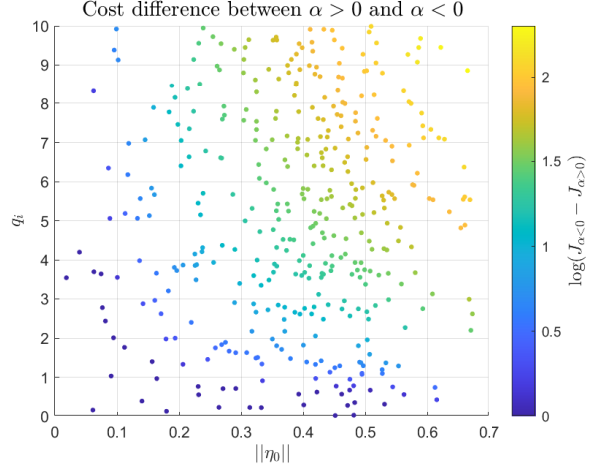


Fig. 11. Cumulative cost difference between  $\alpha = |\bar{\alpha}| > 0$  and  $\alpha = -|\bar{\alpha}| < 0$  for simulations of the nonlinear system in (5) for different initial conditions and cost functions, showing that  $\alpha > 0$  is always better for the simulated cases, using the `ode45` solver in MATLAB, for  $|\bar{\alpha}| = 0.55$ .

## 6 Conclusion

This paper examines the impact of the position of a rigidly attached heavy payload on the closed-loop stability and disturbance rejection performance for a multirotor UAV, in case an arbitrary point on the UAV needs to be controlled accurately. Using a complete nonlinear Euler-Lagrange model of the UAV with payload, we showed how the zero dynamics are unstable when the signed distance between the to-be-controlled Point of Interest  $POI$  and total Center of Gravity  $CoG$ , indicated as  $\alpha = z_{POI} - z_{CoG}$  is negative and how the linearized zero dynamics are marginally stable when  $\alpha$  is positive.

A direct implication is that, if the payload is the controlled output position, placing the payload above the original Center of Gravity of the UAV  $CoG_{UAV}$  is preferred in terms of stability. Future work includes proving Lyapunov stability for the non-linearized zero dynamics

By linearizing the model around the hovering point (which is the relevant state for many heavy-payload applications), we derived an analytical expression for the  $\mathcal{H}_2$ -norm, representing the attenuation of white noise input disturbances on the outputs of the system. This allows us to derive an optimal value for  $\alpha$ , given by  $\alpha^* = \sqrt{\frac{2g}{q_i}}$  for the best white noise input disturbance rejection capabilities, where less control authority results in a higher optimal value for  $\alpha$ , indicating the controlled point of interest should be placed higher.

Although practicalities, such as design space restrictions or application-based constraints, could weigh heavier than the indicated performance improvement, this analysis gives a better intuition on how to place components

on a multirotor UAV.

## References

- [1] Taha Benarbia and Kyandoghere Kyamakya. A Literature Review of Drone-Based Package Delivery Logistics Systems and Their Implementation Feasibility. *Sustainability*, 14(1):360, January 2022. Number: 1 Publisher: Multidisciplinary Digital Publishing Institute.
- [2] Francesco Betti Sorbelli. UAV-Based Delivery Systems: A Systematic Review, Current Trends, and Research Challenges. *ACM J. Auton. Transport. Syst.*, 1(3):12:1–12:40, 2024.
- [3] Stephen Boyd, Laurent El Ghaoui, Eric Feron, and Venkataraman Balakrishnan. *Linear Matrix Inequalities in System and Control Theory*. Studies in Applied and Numerical Mathematics. Society for Industrial and Applied Mathematics, January 1994.
- [4] Pierre-Jean Bristeau, Philippe Martin, Erwan Salaün, and Nicolas Petit. The role of propeller aerodynamics in the model of a quadrotor UAV. In *2009 European Control Conference (ECC)*, pages 683–688, August 2009.
- [5] Jaime del Cerro, Christyan Cruz Ulloa, Antonio Barrientos, and Jorge de León Rivas. Unmanned Aerial Vehicles in Agriculture: A Survey. *Agronomy*, 11(2):203, February 2021. Number: 2 Publisher: Multidisciplinary Digital Publishing Institute.
- [6] Herbert Goldstein, Charles P. Poole, and John L. Safko. *Classical mechanics*. Pearson [u.a.], Upper Saddle River, N.J, 3. ed., internat. ed. [nachdr.] edition, 2007.
- [7] Roger A. Horn and Charles R. Johnson. *Matrix Analysis*. Cambridge University Press, Cambridge, 1985.
- [8] Amal Al Hulaibi, Hawraa Wahid, Salem Al Saif, Jumanah Sadeq, Seyed Esmaeili, and Marwa Kandil. SkyBot - A Novel Autonomous Window Cleaning Drone. In *2023 International Conference on Electrical, Communication and Computer Engineering (ICECCE)*, pages 1–6, December 2023.
- [9] Alberto Isidori. The zero dynamics of a nonlinear system: From the origin to the latest progresses of a long successful story. *European Journal of Control*, 19(5):369–378, September 2013.
- [10] Jeongeon Kim, Seungwon Kim, Chanyoung Ju, and Hyoung Il Son. Unmanned Aerial Vehicles in Agriculture: A Review of Perspective of Platform, Control, and Applications. *IEEE Access*, 7:105100–105115, 2019.
- [11] de Kraker, A. and van Campen, D.H. *Mechanical vibrations*. Shaker-Verlag, Maastricht, 2001.
- [12] KTV. High rise window, facade and building cleaning with a drone.
- [13] Hyunyong Lee, Yu Min Hwang, Jungi Lee, Nac-Woo Kim, and Seok-Kap Ko. A Drone-Driven X-Ray Image-Based Diagnosis of Wind Turbine Blades for Reliable Operation of Wind Turbine. *IEEE Access*, 12:56141–56158, 2024.
- [14] Vincenzo Lippiello and Fabio Ruggiero. Cartesian Impedance Control of a UAV with a Robotic Arm. *IFAC Proceedings Volumes*, 45(22):704–709, January 2012.
- [15] Bas Meere, Sander Doodeman, Franck P. Vidal, Paula Chanfreut, Elena Torta, and Duarte Antunes. X-ray Image Generation for Robotic Radiography: a Case Study on Motion Blur in Drone-Based Wind Turbine Inspections. *Journal of Nondestructive Evaluation*, 44(4):139, October 2025.
- [16] Javier Molina and Shinichi Hirai. Dynamic landing gear for balancing a multirotor helicopter. In *2017 International Conference on Unmanned Aircraft Systems (ICUAS)*, pages 1731–1736, June 2017.
- [17] Hai-Nguyen Nguyen, ChangSu Ha, and Dongjun Lee. Mechanics, control and internal dynamics of quadrotor tool operation. *Automatica*, 61:289–301, November 2015.
- [18] Anibal Ollero, Guillermo Heredia, Antonio Franchi, Gianluca Antonelli, Konstantin Kondak, Alberto Sanfelix, Antidio Viguria, J. Ramiro Martinez-de Dios, Francesco Pierri, Juan Cortes, Angel Santamaria-Navarro, Miguel Angel Trujillo Soto, Robin Balachandran, Juan Andrade-Cetto, and Angel Rodriguez. The AEROARMS Project: Aerial Robots with Advanced Manipulation Capabilities for Inspection and Maintenance. *IEEE Robotics & Automation Magazine*, 25(4):12–23, December 2018.
- [19] Zizhen Ouyang, Ruidong Mei, Zisen Liu, Mingxin Wei, Zida Zhou, and Hui Cheng. Control of an Aerial Manipulator Using a Quadrotor with a Replaceable Robotic Arm. In *2021 IEEE International Conference on Robotics and Automation (ICRA)*, pages 153–159, May 2021. ISSN: 2577-087X.
- [20] Ayush Raina, Nakka , Sanket, Bansal , Mukul, Desai , K. A., Shah , S. V., , and C. Venkatesan. Automated configuration design framework for payload integration in unmanned aerial vehicles. *Engineering Optimization*, 54(12):2017–2033, December 2022. Publisher: Taylor & Francis \_eprint: <https://doi.org/10.1080/0305215X.2021.1971212>.
- [21] Davi A. Santos and José A. Bezerra. On the control allocation of fully actuated multirotor aerial vehicles. *Aerospace Science and Technology*, 122:107424, March 2022.
- [22] Endre Süli and David F. Mayers. *An Introduction to Numerical Analysis*. Cambridge University Press, August 2003. Google-Books-ID: hj9weaqJTBQC.
- [23] J. Willems. Least squares stationary optimal control and the algebraic Riccati equation. *IEEE Transactions on Automatic Control*, 16(6):621–634, December 1971.
- [24] Yue Tan Zhang, Jin Tuan Zhang, Yue Liu, Kun Liu, and QiPeng Wang. Spray-on steady-state study of multi-rotor cleaning unmanned aerial vehicle in operation of photovoltaic power station. *Energy Reports*, 11:5638–5653, June 2024.
- [25] Kemin Zhou, John Comstock Doyle, and Keith Glover. *Robust and Optimal Control*. Prentice Hall, 1996. Google-Books-ID: RPSOQgAACAAJ.